Fabrication of magnetic helical microribbons made of nickel thin films sandwiched between silicon nitride layers for microswimming applications

OPEN ACCESS
IOP Publishing
Nanotechnology

Nanotechnology **34** (2023) 015301 (12pp) https://doi.org/10.1088/1361-6528/ac9530

Fabrication of magnetic helical microribbons made of nickel thin films sandwiched between silicon nitride layers for microswimming applications

Milad Shojaeian[1], Hakan Osman Caldag[2], Ayhan Bozkurt[3] and Serhat Yesilyurt[4]

[1] Department of Mechatronics Engineering, Sabanci University, 34956 Istanbul, Turkey
[2] Department of Mathematics, University of York, YO10 5DD, York, United Kingdom
[3] Electronics Engineering Department, Sabanci University, 34956 Istanbul, Turkey
[4] Sabanci University Nanotechnology Research and Application Center, 34956, Istanbul, Turkey

E-mail: hakan.caldag@york.ac.uk

Received 12 May 2022, revised 17 September 2022
Accepted for publication 27 September 2022
Published 12 October 2022

Abstract

Helical swimming is adopted by microswimming robots since it is an efficient mechanism and commonly observed among microorganisms swimming at low Reynolds numbers. However, manufacturing of micro-helices made of sub-micron magnetic thin layers is neither straightforward nor well-established, advanced materials and methods are necessary to obtain such structures as reported in the literature. In this paper, a topological patterning method utilizing basic microfabrication methods is presented for the self-assembly of magnetic micro-helices made of a sandwiched nickel thin film (50–150 nm) between two silicon nitride layers. Strain mismatch between the thin films and the geometric anisotropy introduced by the slanted patterns on the top nitride layer result in self-rolled-up helical microribbons. Moreover, inspired by the actual release process during the wet-etching of the microribbon from the substrate, moving boundary conditions are incorporated in a numerical model to simulate the self-rolling of trilayer ribbons. The simulation results are compared and validated by experimental data within 7% error for all cases, including the geometries that do not result in a helical shape. The swimming performance of the magnetized micro-helix is demonstrated inside a capillary glass tube experimentally and cross-validated with a numerical model.

Supplementary material for this article is available online

Keywords: microfabrication, self-scrolling, artificial microswimmers, finite-element modelling

(Some figures may appear in colour only in the online journal)

1. Introduction

Magnetic micro-helices have a remarkable potential to be useful in biomedical applications as efficient, fuel-free and remotely controllable structures with high tow-capacity [1, 2]. Mimicking the propulsion mechanisms of microorganisms [3] and owing to the widespread use of magnetic fields in biomedical applications, they are the prime candidates for potentially revolutionary microrobotic applications in medicine and biology, such as artificial insemination [4], boosting the immune response [5], opening of clogged arteries [6] and intraocular surgery [7]. At micro scales, reciprocal motion

mechanisms, like swimming of fish, are not effective to obtain net displacement since the Reynolds number is too small [1, 8]. Hence it is not a surprise to observe the 'cork-screw' motion, i.e. propulsion by means of rotation of a helical tail, as the predominant mechanism of locomotion among the microorganisms, such as *E. Coli*, spriochetes and spermatozoa [9–11]. Inspired by the natural prevalence of cork-screw motion, magnetized helical microswimmers with a helical tail are studied extensively for controllable microswimming in recent years [12–16].

A broad range of methods has been developed to fabricate micro-helices, including 3D-printing [17–19], laser micromachining [20], template-assisted fabrication [5, 13, 21], glancing angle deposition [22], and electrospinning [23]. Moreover, self-assembly microfabrication techniques, such as self-rolling due to initial strain mismatches between layers of thin films and a substrate have received special attention in producing 3D structures such as tubes and helical ribbons [24–27]. Rolling direction of the thin film determines the final shape after the release of the structure from the substrate. In crystalline thin films, the anisotropic distribution of mechanical properties is exploited to fabricate rolled-up helical ribbons by arranging the misalignment of a bilayer or multilayer patterns with respect to the crystalline orientation of the substrate [12, 28–30]. On the other hand, strain-induced noncrystalline, polycrystalline, or nanocrystal nanomembranes, in which the mechanical properties are deemed to be isotropic, can be rolled up in an arbitrary orientation (i.e. long side rolling, short side rolling, or mixed rolling) based on the geometry, strain mismatch, mechanical properties, and the etching process [25, 31]. In such cases, one needs to induce anisotropy (e.g. anisotropic driving force, or bending stiffness) by modifying the 2D geometry of the thin film or by introducing patterns in the thickness direction. This approach has been demonstrated with monolayer titanium micro springs with well-defined helical angles by using a grated sublayer underneath the metal ribbon with an orientation angle between the edge-wise directions of the ribbon and the grating [26]. In another study, monolayered helical ribbons were formed when the tips of narrow stripes of nanocrystalline diamond nanomembranes were shaped as a 'utility-knife' [27]; and helical structures were obtained when 'hockey-stick'-shaped monolayered stripes were released by under-etching [32].

Silicon nitride (SiN_x) thin films have favourable properties such as biocompatibility [33]; oxidation, corrosion and electrical resistivity; as well as thermal and chemical stabilization [34, 35]. Moreover, they have been utilized in the self-assembly fabrication of rolled-up multilayers for various applications [36–40] by exploiting the strain gradients that develop during deposition. Strain gradients originate from the deposition of SiN_x at different plasma excitation frequencies in a plasma-enhanced chemical vapor deposition (PECVD) device. At high frequencies, the ions in the chamber do not respond to the radio frequency (RF) field so the deposited layer is not as dense and tensile intrinsic stresses develop within the layer [41]. At low frequencies, however, the ions respond to the RF and this leads to ion bombardment on the deposited surface, causing intrinsic compressive stresses to build up [41]. Optimizing for maximum stresses, it is found that an operation frequency of 13.56 MHz results in a (tensile) stress value of 406.95 MPa while an operation frequency of 380 kHz results in a (compressive) stress of −1168 MPa [36]. When the strained structure is released from the substrate, it rolls up by itself in a direction determined by its geometry [27] or alignment of the structure with respect to the crystal orientation of the substrate [40]. On the other hand, evaporated nickel is a ferromagnetic material commonly used for magnetizing swimming microrobots [13, 42–46]. However, this material is toxic for medical applications [46] and susceptible to oxidation in aqueous environments [19]. Combining SiN_x with Ni assists one to take advantage of both material properties at the same time with promising functionalities specifically in biomedical applications.

This work reports helical, magnetized microribbons for microswimming applications. In literature, microswimmers are manufactured by using either advanced materials such as InGaAs/GaAs bilayer ribbons attached to a head made of Ni [12] or advanced methodologies such as glanced angle deposition [14] and direct laser writing [13], followed by coating them with magnetic materials such as Co and Ni/Ti, an excellent recent review article discusses the key features of various manufacturing methods [2]. Here, we propose to manufacture a magnetic helical microribbon by self-scrolling of a trilayer structure that sandwiches a Ni nanolayer between low-frequency (LF) and high-frequency (HF) SiN_x nanolayers. Since both SiN_x and Ni are expected to have isotropic properties [30, 40, 47–50], grating the top SiN_x layer with oblique patterns at specific angles introduces the necessary anisotropy unlike in other studies where the patterns are etched onto the substrate and monolayer or bilayer films are deposited on top [26]. Self-rolling leads to micro-helices or irregular helical shapes depending on the geometric parameters of the oblique patterns. An extensive characterization process is carried out to investigate the effects of the size, depth, and the angle of orientation of the surface patterns on scrolling for fixed length, width and thickness of the layers. Moreover, a quasi-static finite-element model (FEM) is developed to analyze the self-rolling process during the release of the structure from the substrate using a unique set of boundary conditions consistent with experimental observations. The simulation results demonstrate excellent agreement with experiments both for the helical and non-helical structures obtained from the microfabrication experiments. According to the FEM, the final shape is determined by the minimization of the elastic energy in the structure.

We demonstrate the utility of the proposed design as a magnetically actuated microswimming robot. The proposed design has several key advantages in the scope of microrobotic applications. The ribbons are magnetic because of the Ni layer, so attachment of a separate magnetic head [46] or Ni–Ti bilayer coatings [4, 51] are not necessary. The lack of a head, combined with the fact that the heavy magnetic material is distributed evenly in the structure, is advantageous in terms of controlled navigation as the head is shown to tilt the swimmer down, which would require additional control strategies for gravity

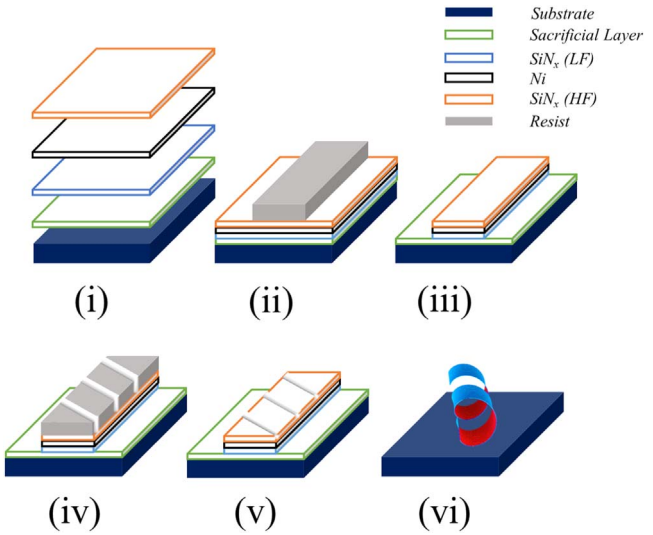

Figure 1. Process flow of fabricating self-rolled up helical structure: (i) bottom-up deposition, (ii) first lithography, (iii) consecutive RIE, wet etching, and RIE, (iv) second lithography, (v) RIE for revealing the grating patterns on the ribbon and (vi) final wet etching that gives the helix. Grating patterns are shown in white for visual clarity.

compensation. [12, 52]. The symmetry in the structure eliminates different trajectories observed in swimmers with a head when they move in the head or tail direction [53]. Another advantage is the structural rigidity enabled by the Ni layer distributed all over the swimmer: This allows the structure to retain its helical shape for a long time as the residual stresses that lead to the helical rolling do not relax over time. Lastly, the Ni layer, known to be toxic, is sandwiched in-between the SiN_x layers so that exposure to the outer media is limited which also significantly limits the probability of corrosion in fluids and improves biocompatibility. We used a Helmholtz coil setup to rotate the manufactured helical microribbon inside a capillary glass tube filled with IPA, carried out experiments at different rotation frequencies to demonstrate the swimming performance, developed a three-dimensional computational fluid dynamics (CFD) model to compare the swimming velocities with simulation results, and, lastly, studied the effects of the width and wavelength on the swimming velocity of the ribbon using the CFD model.

2. Methods

2.1. Fabrication of the microswimmers

The process flow of fabrication is depicted in figure 1. A 4 inch p-type ⟨100⟩ orientation Si wafer with 1 μm thermally grown SiO_2 layer is used as the substrate. As the first process step, a 250 nm thick chromium (Cr) sacrificial layer is deposited using an e-beam physical vapor deposition (PVD) system (Torr International Services LLC, Marlboro, NY) at a deposition rate of 2.5 Å s^{-1}, and a pressure of 5×10^{-6} mTorr. While lower sacrificial layer thicknesses are more preferable to reduce the duration of its etching, we observed the ribbon sticking to the surface of the substrate due to the capillary forces, preventing self-scrolling or causing non-helical structures to form. That is why we increased the layer thickness up to 250 nm. One cannot increase the thickness indefinitely as the etchant selected for Cr (see below) also attacks the Ni layer (see section SI in supplemental material for details). Following the PVD, a thin film of LF-SiN_x is deposited with a thickness of 160 nm by PECVD using the proprietary recipe of OXFORD Plasma Pro100 Process Module with the following parameters: temperature = 300 °C, power = 20 W, pressure = 650 mTorr, frequency = 380 kHz, 5% SiH_4/N_2 = 400 sccm, NH_3 = 20 sccm, and N_2 =600 sccm. Third, a 50 nm thin layer of nickel is deposited using the e-beam evaporator with the same conditions as in the deposition of the sacrificial layer. Finally, a thin film of HF-SiN_x is deposited with a thickness of 310 nm by the PECVD method with the same recipe as LF-SiN_x at a frequency of 13.56 MHz (see figure 1(i)).

Ribbons on the sandwiched nanomembrane are patterned by photolithography using a Midas MDA-60MS mask aligner (Midas System Co, Ltd, Yuseong-gu, Daejeon). First, a Microchemicals AZ5214E photoresist film is spin-coated, followed by a pre-bake of 1 min at 105 °C on a hot plate. After that, a light-field mask with rectangular patterns with different orientation angles is used for patterning. Subsequently, the sample undergoes a developing process in AZ 726 MIF developer for 50 s (see figure 1(ii)). The ribbon patterns are etched through the HF-SiN_x layer at 90 s by reactive ion etching (RIE) with the use of OXFORD Plasma Pro100 device with the following recipe: temperature = 20 °C, pressure = 10 mTorr, SF_6 = 20 sccm, CHF_3 = 80 sccm, RF power = 50 W, and ICP power = 2000 W. The measured etch rate is around 4 nm s^{-1}. As this is the first patterning step that reveals the ribbons, one needs to go through all three layers of the material. That is why we follow with a wet etching process for the nickel layer by $FeCl_3$ 85%/DI-water etchant with a ratio of 1:20 for around 15 s. Finally, using RIE with the same recipe described above at 50 s, the LF-SiN_x is etched away to reach the Cr sacrificial layer (see figure 1(iii)).

In order to create the second pattern on the ribbons that determines the direction of rolling (the grating pattern), another lithography process is performed with a different mask that has the grating patterns on it (see figure 1(iv)). The process parameters of lithography are exactly the same as the previous one. This step is followed by RIE (see figure 1(v)) to etch away the top layer partially at different depths, characterized by H/T (see figures 2(a) and (b) for the geometric description of the parameters). RIE duration varies depending on the depth of the grating pattern.

After cleaning the resist, the sample is immersed into chromium etchant TechniEtch Cr01 to allow the patterned ribbons to be detached from the substrate and form helical ribbons (see figure 1(vi)). The geometric dimensions of the helix are given in figure 2(c). It is worth mentioning that a detailed cleaning procedure is carried out in-between each RIE and wafer scribing by immersion of the sample into hot acetone at 40 °C for about 3 min followed by sonication in water, isopropyl alcohol (IPA), DI-water rinsing, and finally

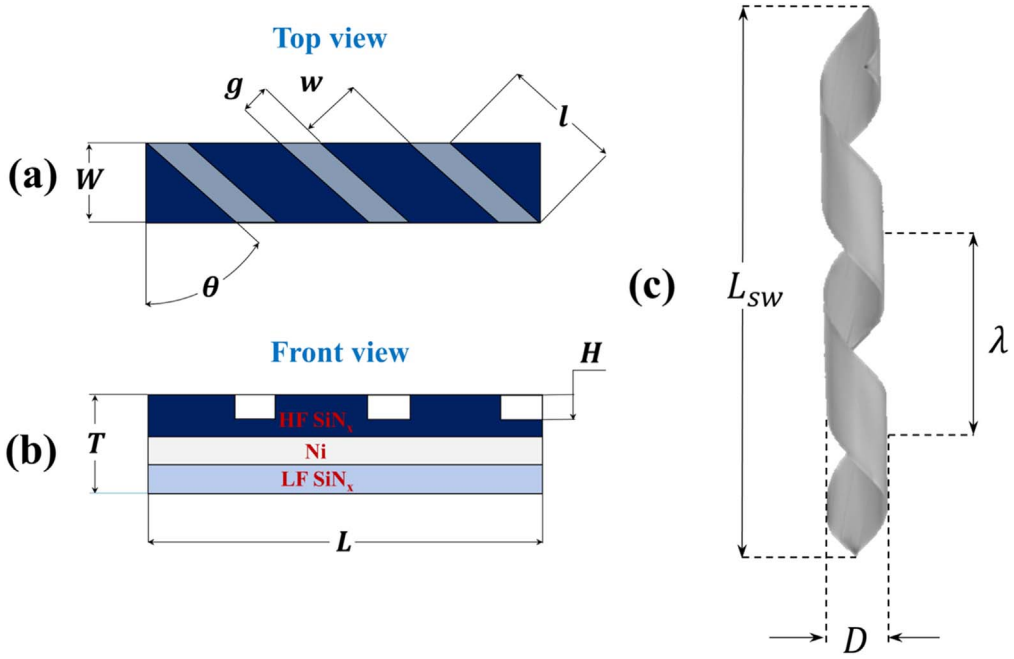

Figure 2. (a) Top and (b) front views of the ribbon before the wet etching process (i.e. before self-scrolling), showing critical geometric parameters. (c) The helical swimmer geometry and its parameters.

Table 1. The base geometric parameters for the fabrication experiments.

Geometric parameter	Value
L (μm)	1050
W (μm)	120
t_{LF} (nm)	160
t_{Ni} (nm)	50
t_{HF} (nm)	310

drying process using nitrogen gas as our initial trials resulted in failure even from very low amounts of contamination on the surface of the substrate. Further details on the microfabrication, including information on the thickness and stress measurements and etchant selection, are provided at section SI in the supplemental material.

The base geometric parameters used in the fabrication experiments are provided in table 1. Determination of the base parameters involved many trials with experiments and simulations. As an example, for SiN_x thicknesses less than 100 nm, pinholes appeared on the substrate that completely ruin the ribbons during the etching step, so we had to work with thickness values larger than this value. The thickness of Ni layer, on the other hand, is mainly determined by the strength of the actuating magnetic field applied to the swimmer. Lastly, one other aspect we considered was to fabricate swimmers with $D \sim W$ for convenience. These three factors contributed to the reference dimensions in this work.

2.2. The finite-element model

The rolling behaviour of the tri-layer nanomembranes during the etching process is investigated further with the help of a three-dimensional FEM model based on a quasi-static approach using COMSOL Multiphysics v5.6. Solid mechanics module is used in modelling the deformation of the nanomembranes. Due to large deformations, geometric nonlinearity is considered in the model, resulting in the following governing equations for a fully elastic, stationary study:

$$\mathbf{0} = \nabla \cdot (\mathbf{FS}) \tag{1}$$

$$\mathbf{S} = \mathbf{C}\colon \boldsymbol{\epsilon}_{el} \tag{2}$$

$$\boldsymbol{\epsilon}_{el} = \boldsymbol{\epsilon} - \boldsymbol{\epsilon}_{th} \tag{3}$$

$$\boldsymbol{\epsilon}_{th} = \boldsymbol{\alpha}(T - T_{ref}) \tag{4}$$

$$\boldsymbol{\epsilon} = \frac{1}{2}[(\nabla \mathbf{u})^T + \nabla \mathbf{u} + (\nabla \mathbf{u})^T \nabla \mathbf{u}] \tag{5}$$

$$\mathbf{F} = \mathbf{I} + \nabla \mathbf{u} = \mathbf{I} + \frac{\partial \mathbf{u}}{\partial \mathbf{x}} = \begin{bmatrix} 1 + \frac{\partial u}{\partial X} & \frac{\partial u}{\partial Y} & \frac{\partial u}{\partial Z} \\ \frac{\partial v}{\partial X} & 1 + \frac{\partial v}{\partial Y} & \frac{\partial v}{\partial Z} \\ \frac{\partial w}{\partial X} & \frac{\partial w}{\partial Y} & 1 + \frac{\partial w}{\partial Z} \end{bmatrix}, \tag{6}$$

where $\mathbf{S}$, $\boldsymbol{\epsilon}$, $\boldsymbol{\epsilon}_{el}$, $\boldsymbol{\epsilon}_{th}$ represent the second Piola–Kirchoff stress tensor, the strain tensor, elastic strain tensor and isotropic thermal strain tensor, respectively. $\mathbf{C}$ is the elasticity tensor defined by the elastic modulus and Poisson's ratio, $\boldsymbol{\alpha}$ is the isotropic thermal expansion coefficient and $\mathbf{u}$ is the displacement field. T is the temperature and $\mathbf{F}$ is the transformation matrix that represents large deformations. The self-scrolling is induced by the stress anisotropy in different layers of the ribbon. The average measured stresses inside LF-SiN_x, Ni, and HF-SiN_x layers are obtained as -1444.7 MPa, 518.8 MPa and 277.3 MPa, respectively; these values are

Table 2. Material properties assigned in the FEM model.

Thin film	Elastic modulus (GPa)	Poisson's ratio	Thermal expansion coefficient (1/°C)	Temperature (°C)
LF-SiN_x	210	0.28	2.75e-6	1820
Ni	200	0.31	−7.75e-7	2300
HF-SiN_x	210	0.28	−5.20e-7	1820

realized in the model by setting arbitrary thermal expansion coefficients and temperature differences. This induces some additional strain (via ϵ_{th}) that gives the desired intrinsic stresses in the layers. Since the stress level in each layer is different, the imposed coefficients are different even between the two SiN_x layers. We assume that the intrinsic stresses are isotropic based on the other studies in the literature [30, 40, 47–50], experiment results and profilometry measurements given in section SI in Supplemental Material. The list of the corresponding mechanical properties is given in table 2.

The scrolling of the ribbon after release from the substrate is modelled by applying moving boundary conditions with a quasi-static approach. Inertial effects are neglected due to the low mass of the thin-film and strong viscous effects during the wet etching process. As the sacrificial layer is etched from below the trilayer nanomembrane, the initial phase of the release of the structure would be as shown in figure 3(a), starting at the same time from all edges and moving towards the center of the ribbon with a length of L and width of W. To mimic this behavior in the simulation environment, we use moving boundary conditions by fixing the bottom surface of the membrane only in the region which is smaller than the whole surface by a distance, s, and increase the value of s gradually at each step all the way to the red line shown in the figure. One would expect the etching to continue this way until the center of the ribbon is released, shown as a green dot in figure 3(a). However, as previously mentioned for polymers and semiconductors, the aspect ratio [25, 31] and the wrinkling modes [54, 55] of the ribbon can affect the rolling behavior of the structure. This can be clearly seen from figure 3(b) for an LF-SiN_x/HF-SiN_x bilayer; at $L/W = 4$, where the circumference (C) is comparable to the width and thus long side rolling is energetically more favorable [25, 31]. However, once the aspect ratio scales up to 8 (figure 3(c)), the behavior of the bilayer changes. In this situation, the structure is rolled up from the long edge but it has not attained its final shape since it initially adheres to the substrate due to capillary force, and then changes its rolling direction to the diagonal of the ribbon. As a result, the structure enters an unstable state which abruptly snaps to form a compacted helical structure. A possible explanation for this are the wrinkling modes which are more pronounced in structures with very high aspect ratios where the circumference is comparable to the width. At a lower aspect ratio, as depicted in figure 3(b), the wrinkling modes become flattened to proceed with long side rolling before the structure is fully released. However, at a higher aspect ratio, where even a single turn of rolling does not occur, the wrinkling affects the deformation before fully releasing from the substrate. The elastic energy history shown in figure 4(a) confirm this behavior. Furthermore, we carry

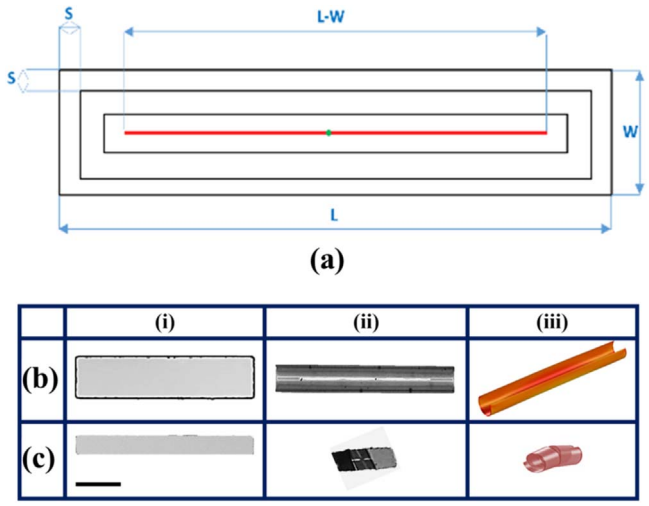

Figure 3. (a) Schematic view of the isotropic etching process. (b) and (c) demonstrate the effects of the aspect ratio on the rolling behavior. At (b), $L/W = 4$, and $C/W = 1.4$; and at (c) $L/W = 8$, $C/W = 2.8$. (i) and (ii) are the images of the ribbon from experiments before and after releasing, respectively, and images at (iii) are the corresponding simulation results (scale bar size is 200 μm).

out an etching process for a bilayer SiN_x nanomebrane and follow how it is released from the surface during the etching process. Since SiN_x is transparent, one can easily observe how the structure is released from the substrate. The images at figure 4(b) show captures from this etching process, confirming the diagonal rolling. However, as shown in the final frame in figure 4(b), the structure forms a compacted helical shape after release. When we test out a ribbon with Ni layer, shown in Video S1 in supplemental material, the ribbon follows the same steps and this time forms a perfect helix, even if the C/W ratio changes, ranging from 3 to 1. That is why, after the initial 3 steps of release shown in figure 3(a), the fixed boundary conditions are applied along three diagonal equidistant lines with decreasing separation, and the structure is fixed at the center point as the final step to avoid an ill-posed system. The mesh size is set to 1/200 of the total circumference (C) of the rolled-up structure [56] after a detailed convergence analysis.

2.3. Swimming experiments

Figure 5(a) depicts the Helmholtz coils that provide a uniform, rotating magnetic field for the swimming experiments. The setup is reminiscent of those used in practical applications of microswimmers but on a much smaller scale for convenience [57]. The coils have outer diameters of 4 and 6.5 cm for the coils placed in the x- and y- directions,

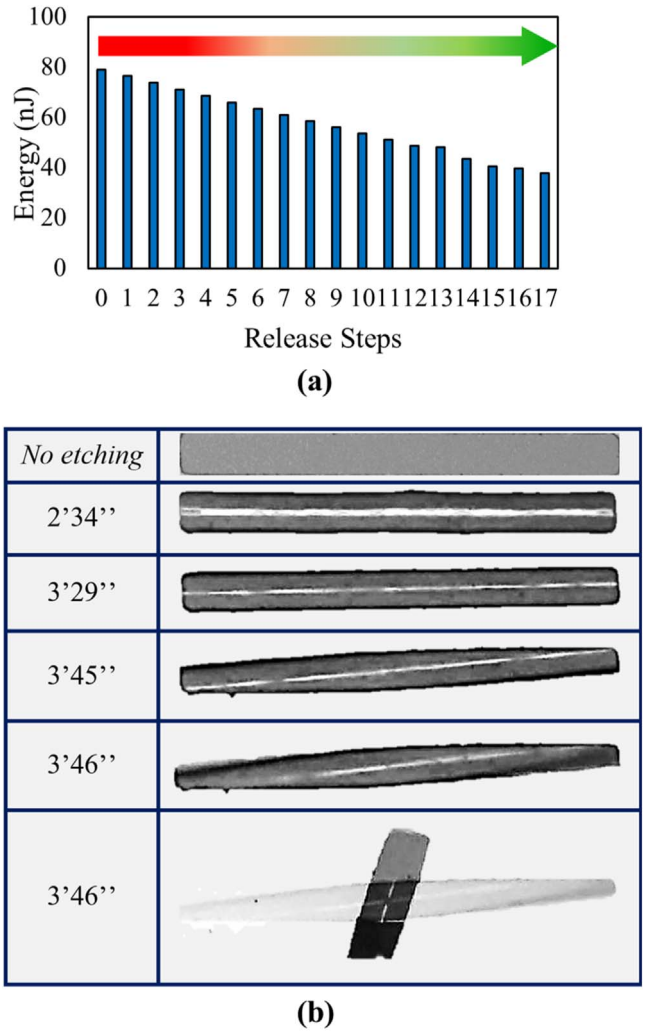

Figure 4. (a) Elastic energy variation for the gradually released nanomembrane with a high aspect ratio. (b) Time-lapse image of releasing and rolling of high aspect ratio nanomembrane consisting of two SiN_x layers. The left column shows the time elapsed after the etching starts.

respectively, suitable for placement under a stereo microscope. The opening in the middle of the top coil allows the recording of the experiments from the top. In accordance with the coordinate frame shown in the same figure, the applied magnetic field is defined as:

$$\mathbf{B} = B_0\left[\cos(\omega t) \quad \sin(\omega t) \quad 0\right]', \tag{7}$$

where $B_0 = 3.6$ mT is the strength of the magnetic field, $\omega = 2\pi f_m$ is the magnetic field angular rotation rate where f_m is the rotation frequency, and t is time. The magnetic field imposes a magnetic torque on the swimmer, given by the equation:

$$\boldsymbol{\tau}_m = \mathbf{m} \times \mathbf{B}, \tag{8}$$

where $\mathbf{m} = V_m\mathbf{M}$ is the magnetization vector of the swimmer that depends on the volume of the magnetic material V_m and magnetic moment $\mathbf{M}$. The actuation mechanism is schematically depicted in figure 5(b). Externally actuated magnetic artificial microswimmers employ either a magnetic coating on the artificial flagella [13, 14] or a magnetic head attached to

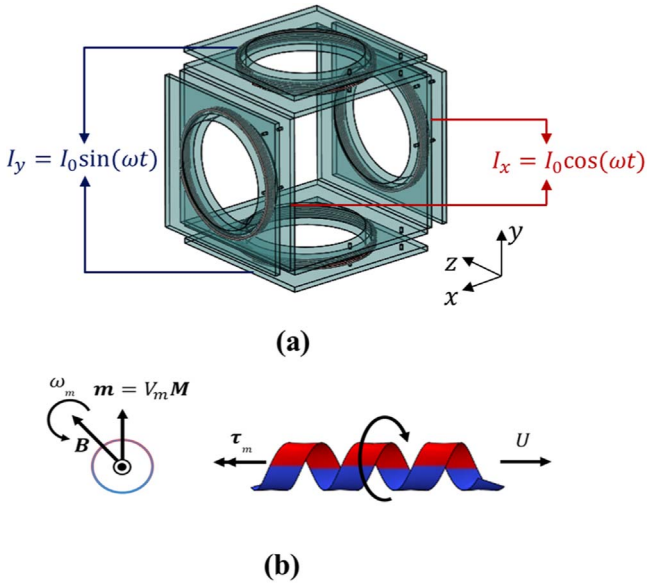

Figure 5. (a) The Helmholtz coil setup with the reference coordinate frame and assigned currents to the coils, (b) magnetic actuation mechanism of the radially magnetized swimmer with a rotating magnetic field on the radial plane.

Table 3. Geometric dimensions of the helical swimmer used in the swimming experiments.

L_{sw} (μm)	D (μm)	λ (μm)	t_{LF} (nm)	t_{Ni} (nm)	t_{HF} (nm)	w/g	H/T	θ (°)
740	60	246	100	150	170	1	0.25	60

the helical tail [12]. In our swimmers, the magnetic material is sandwiched in between two SiN_x layers. This approach has multiple benefits in terms of microswimming applications, which are discussed in section 1.

In experiments, swimmers with total length L_{sw}, diameter D and wavelength λ (complete set of dimensions are provided in table 3) are placed in glass tubes filled with isopropyl alcohol and propelled with the Helmholtz coils. Note that the thickness of the Ni layer is increased from 50 to 150 nm for stronger magnetization and enabling swimming under weaker magnetic fields. We have followed the guidelines established from our fabrication experiments to determine the critical pattern parameters w/g, H/T and θ in table 3, showing that the guidelines proposed here can be used to manufacture swimmers with different layer thicknesses. Coil currents I_x and I_y with the amplitude I_0 are provided by Maxon ADS_E 50/5 motor drivers and NI DAQ hardware. A MATLAB user graphical interface is designed to control the current and f_m. An optical microscope (Nikon SMZ1270) equipped with a camera (Basler acA2440-75um) is used to record swimmer motion. The frame rate of the recording is fixed at 25 FPS, and the contrast of the images is adjusted properly to make the subsequent image-processing straightforward. As a post-processing step, the recorded videos are collected and analysed through an image processing procedure whose details can be found in [53]. Average swimming velocities are

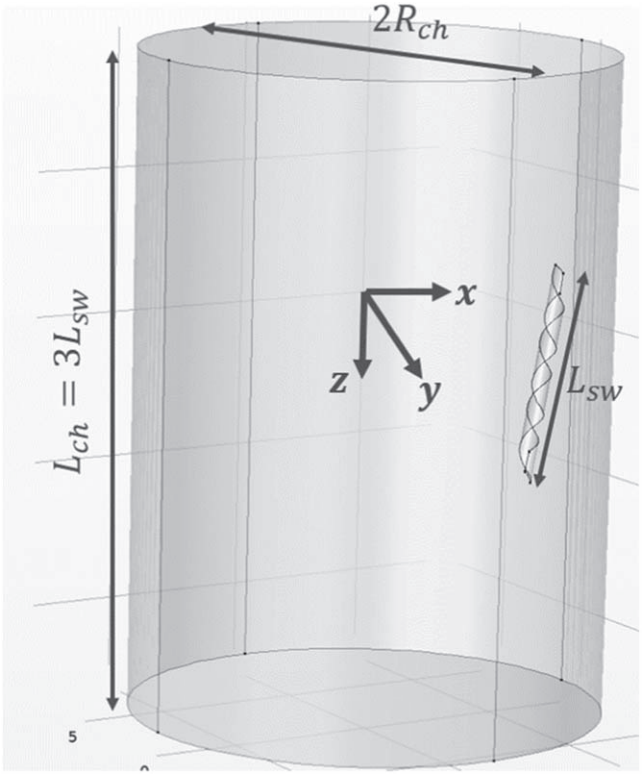

Figure 6. The geometric setup for the computational fluid dynamics model.

obtained by linear curve fitting to position data and the variation of velocity is found from the root mean square error of the fit line.

2.4. Computational fluid dynamics modelling for the swimming experiments

The velocity of the helical swimmer is obtained from the solution of the Stokes' equations for the flow due to the rotation and translation of the swimmer inside a cylindrical channel. The equation is given by:

$$\mu\nabla^2\mathbf{u}_f - \nabla p_f = 0, \quad \nabla \cdot \mathbf{u}_f = 0, \tag{9}$$

where $\mathbf{u}_f$ is the fluid velocity field and p_f is fluid pressure and μ is the viscosity of the fluid, which is isopropyl alcohol (IPA) with $\mu = 2.4$ cP. We follow the methodology of the model presented in [58], therefore we take the Reynolds number of the system as zero. The inertial effects at low Reynolds numbers are negligible, so one can solve for the swimming velocities from the steady state solution of the Stokes' equations [58]. The helical swimmer used in the simulations is modelled according to those that we used in the experiments given in table 3.

The swimmer is placed in a channel with the diameter, $2R_{ch} = 1.6$ mm and length $L_{ch} = 3L_{sw}$, which is sufficiently long for the effects of the local flow around the swimmer of length L_{sw} as shown in figure 6. No-slip boundary conditions are applied to channel walls and to the swimmer's surface, where the wall movement is specified by:

$$\mathbf{u}_s = \mathbf{U}_{sw} + \mathbf{R}(\boldsymbol{\omega} \times \mathbf{R}^T(\mathbf{x} - \mathbf{x}_0)). \tag{10}$$

where $\mathbf{U}_{sw}$ is the velocity of the swimmer, $\mathbf{R}$ is the rotation matrix from the swimmer's frame to the channel frame, $\boldsymbol{\omega} = [0 \quad 0 \quad 2\pi]^T$ is the angular velocity of the swimmer rotating around its long axis with angular velocity of 2π for the unitary magnetic rotation frequency. $\mathbf{x}$ is the position at the swimmer's surface and subscript '0' indicates the center of mass of the swimmer. Swimmer velocities for rotations other than $f_m = 1$ Hz are scaled with that frequency. $\mathbf{U}_{sw}$ is obtained by specifying force-free swimming conditions in each direction by integrating the surface force, $\mathbf{n} \cdot \boldsymbol{\sigma}$ over the swimmer surface, Ω_{sw}:

$$\int_{\Omega_{sw}} \mathbf{n} \cdot \boldsymbol{\sigma} dA = 0, \tag{11}$$

where $\mathbf{n}$ is the normal vector on the swimmer surface and $\boldsymbol{\sigma}$ is the stress tensor. In the model, the swimmer is placed at $x = 0.5$ mm with 10° rotations around the y- and x- axes each and the rotation matrix is obtained from the Tait–Bryan angles in that order.

3. Results and discussion

3.1. Characterization of micro-fabricated helices

We first share the characterization results of the scrolling behavior of ribbons with respect to the geometric parameters that define the grating patterns. Four main parameters are considered for the patterns as shown in figure 7(a): g (the gap distance between the islands formed by the grating patterns); w (the width of the islands); H (the depth of the islands); and θ (the angle of the islands). Without any grating applied, as discussed in section 2.2, the structure tends to minimize its energy by forming a compacted helix since its length-to-width ratio is large (greater than 6). Depending on the grating pattern, we observe three distinct final shapes, as shown in figures 7(b)–(d). First, the edges of the rolled-up helical ribbon overlap to form a tubular shape (figure 7(b)) demonstrating that anisotropic effects are not strong enough to form a helix with a sufficient gap between the turns. Second, regular helical structures are obtained (figure 7(c)) when the optimal patterns are used. Lastly, due to excessive local strains and nonuniform mechanical properties, irregular helices are achieved as depicted in figure 7(d) specifically when the depth (H) of the pattern is large, i.e. comparable to the top layer thickness.

A systematic set of experiments are carried out by considering four pattern parameters with the following values: $\theta = 45°$, 50°, and 60°; $H/T = 0.15$, 0.25, and 0.35; $w/L = 0.025$, 0.1, 0.175, and 0.25; and $g/L = 0.025$, 0.05, and 0.075 (check section SII in the supplemental material for the patterned geometries). To ensure the repeatability and accuracy of the results, each experiment is repeated three times. A compact bar chart showing the overall percentage of perfect helices obtained is given in figure 7(e) as a function of g/L and w/L. The effects of H/T and θ are also depicted in figures 7(f)–(h). The results show that lower g/L helps to achieve helical shapes as well as increasing the angle of

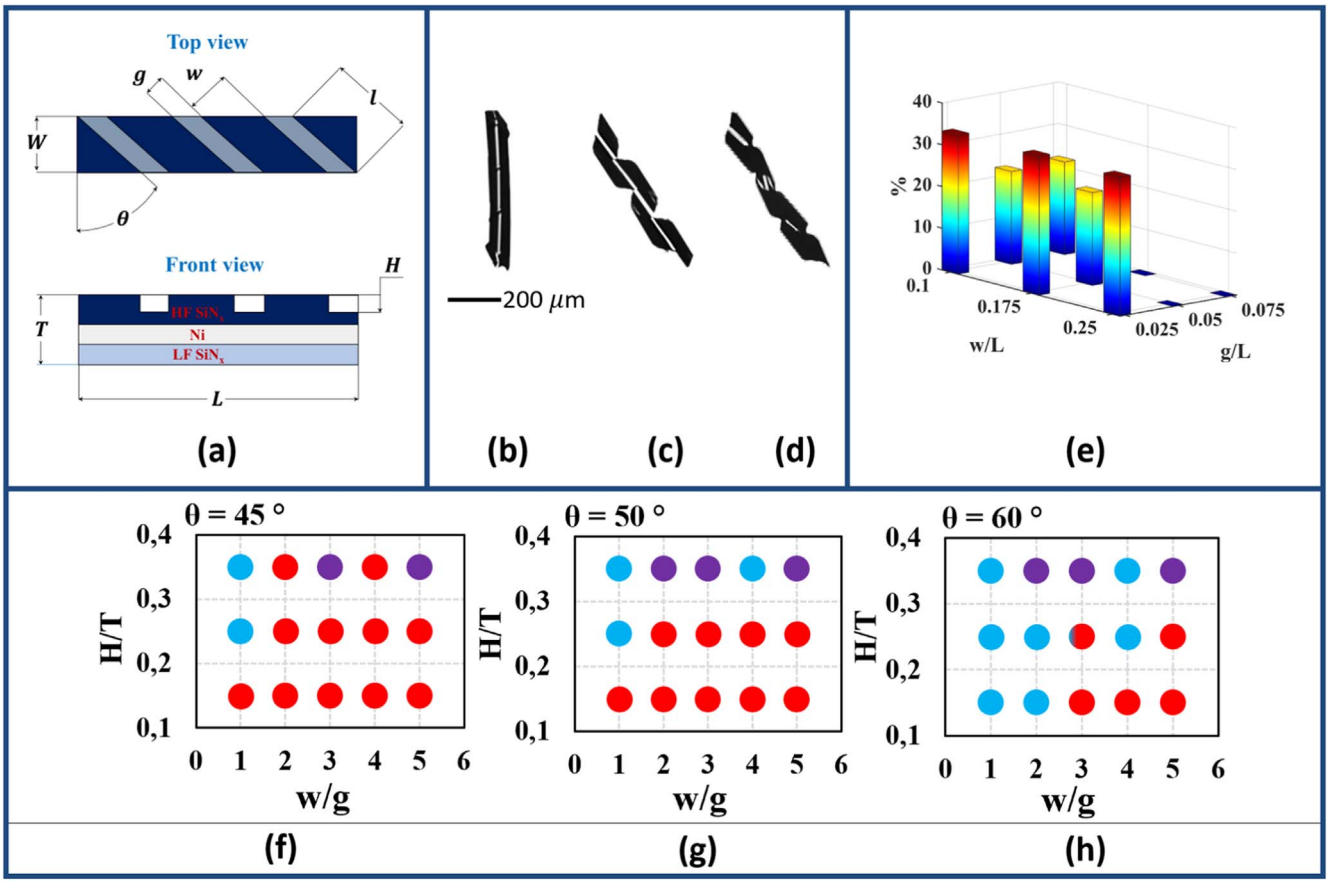

Figure 7. (a) Top and front views of the sandwiched nanolayers; optical microscopic images of the deformed structure as (b) compacted helix, (c) regular helix, and (d) irregular helix; (e) the percentage of generated regular helices for wide islands; and (f)–(h) the scatter graph of resulting helical shapes for 45°, 50°, and 60° pattern angles, respectively. Red dots are for compacted helices, purple dots show irregular helices and blue ones indicate regular helices.

orientation of the pattern and keeping the ratio of w/g close to one. The effect of the depth ratio of the pattern, H/T, is more pronounced at low w/g ratios and high orientation angles. As tabulated in section SII in the supplemental material, for the cases that result in higher helical angles (greater than 75°), where the helical pitch (wavelength) is close to the length of the ribbon, rolled-up ribbons turn into a compacted helical shape abruptly once completely released from the substrate (see video S2 in the supplemental material) even though helical ribbons are observed intermediately before the final release. This behaviour manifests that the final minimum elastic energy level is different from those in intermediate stages when the ribbon is still partially attached to the substrate. In summary, one can infer that at least one of the w/L or g/L ratios has to be kept low enough to obtain helical ribbons. At low length/width ratios of the ribbon, the rolling behaviour of the structure is unpredictable since it can roll up from all sides and keeps rolling in specific directions due to history dependency of the process similar to strain-induced semiconductors and polymer microstructures [25, 31]. However, perpendicular rolling is energetically more favourable for fairly high length/width ratios. Moreover, rolling cannot occur perpendicular to the long edge of the patterns (i.e. l) when the aspect ratio of the patterns, i.e. l/w and l/g are low. Furthermore, for a fixed ribbon length, L, increasing the widths of patterns, either w or g (figure 7), too much reduces the efficacy of patterning, and the rolling direction cannot be controlled as gradually and smoothly, since each section behaves as an individual component.

Optimal g and w values are obtained for the cases when l/w and l/g are moderately high and w/g is low as discussed and predicted for grated single layer and bilayers as well [26, 59]. Accordingly, the effects of patterning depths and angles are elucidated in figures 7(f)–(h) excluding the high values of w/g. At lower depths ($H/T = 0.15$), even if the w/g ratio is low, the effect of the patterning is not notable enough, and, hence, the ribbon tends to roll with a limited helical bias. Increasing the depth ratio to $H/T = 0.25$ gives further bias in the direction and results in better helices. Further increasing the ratio to $H/T = 0.35$ results in a higher difference between the strain gradients and the curvatures of the patterned and unpatterned regions than that of $H/T = 0.25$ leading to predominantly irregular helices [60, 61]. When the pattern angle is 60°, where the aspect ratios of the l/w and l/g are high enough, higher percentage of the structures roll perpendicularly to the long edge of the patterns and higher percentage of smooth helices are formed upon release at optimal patterning values (i.e. low w/g, medium depth, and high angles). In video S1 in supplemental material, the formation of a uniform helix is shown at optimal pattern values.

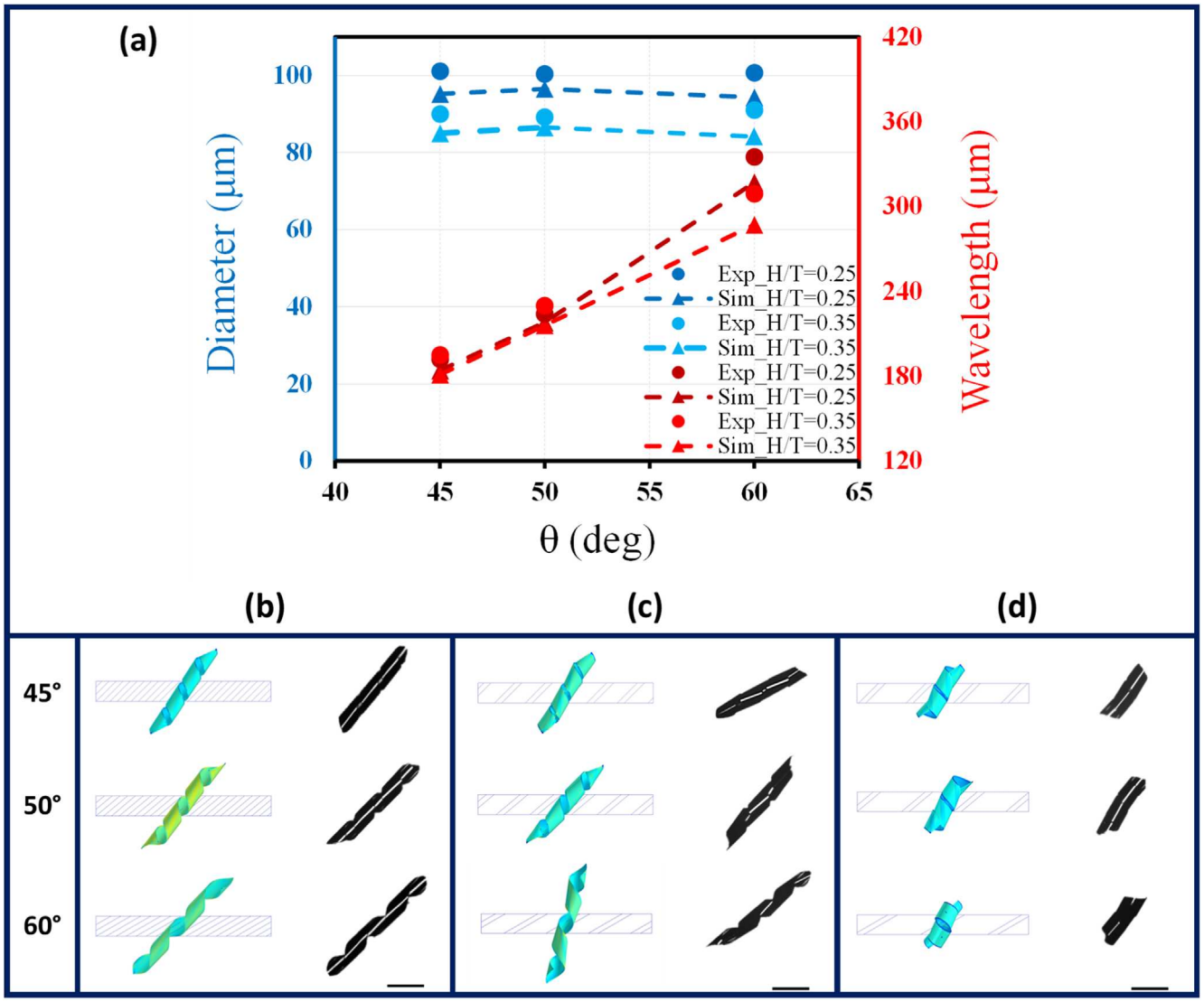

Figure 8. (a) Comparison between experimental and simulation results for patterning parameters of $w/g = 1$ and two depths of $H/T = 0.25$, and 0.35; (b) $w/g = 1$ while $H/T = 0.25$; (c) $w/g = 3$ while $H/T = 0.35$; and (d) $w/g = 5$ while $H/T = 0.25$. The size of the scale bars is 200 μm.

3.2. FEM results

This section provides the validation of the FEM model with various structures obtained from the microfabrication experiments. FEM results are validated quantitatively with the diameters of the rolled-up structures and their wavelengths. Furthermore, we provide qualitative comparisons for the non-helical geometries obtained in experiments. Figure 8(a) depicts the comparison between the helices obtained from experiments and simulations for $H/T = 0.25$ and 0.35, $w/g = 1$, and $\theta = 45°$, 50° and 60°. The average diameter of the helices remains constant as predicted by simulations as well with an average error of around 5%. Helical pitch angle, β, increases with the orientation angle as in the case of monolayers [26]; thus, the helical wavelength, λ, increases with the pattern orientation, θ, satisfying the relationship between the geometric parameters of the helix, $\lambda = \pi D \tan\beta$, where D is almost constant since the geometric parameters of the tri-layer thin film are fixed. Moreover at higher grating depth, $H/T = 0.35$, the thickness of the top layer varies considerably more between the grated and untouched portions than for $H/T = 0.25$. As a result, the final ribbons have about 10% smaller diameter and helical wavelength for $H/T = 0.35$ than for $H/T = 0.25$. Overall, simulation results agree well with experimental observations with an average error of around 7%. Additional comparisons are shown in figures 8(b)–(d) for further confirmation of the agreement between experiments and simulations; uniform helices with varying pitch angles are shown in figure 8(b), irregular helices in figure 8(c), and compacted helices where the edges overlap are illustrated in figure 8(d).

3.3. Swimming experiments

The micro-helices are placed in a magnetic actuation setup as described in section 2.3 and the swimming trajectories are recorded with different f_m, ranging from 1 to 20 Hz. Each swimming experiment is repeated three times for consistency

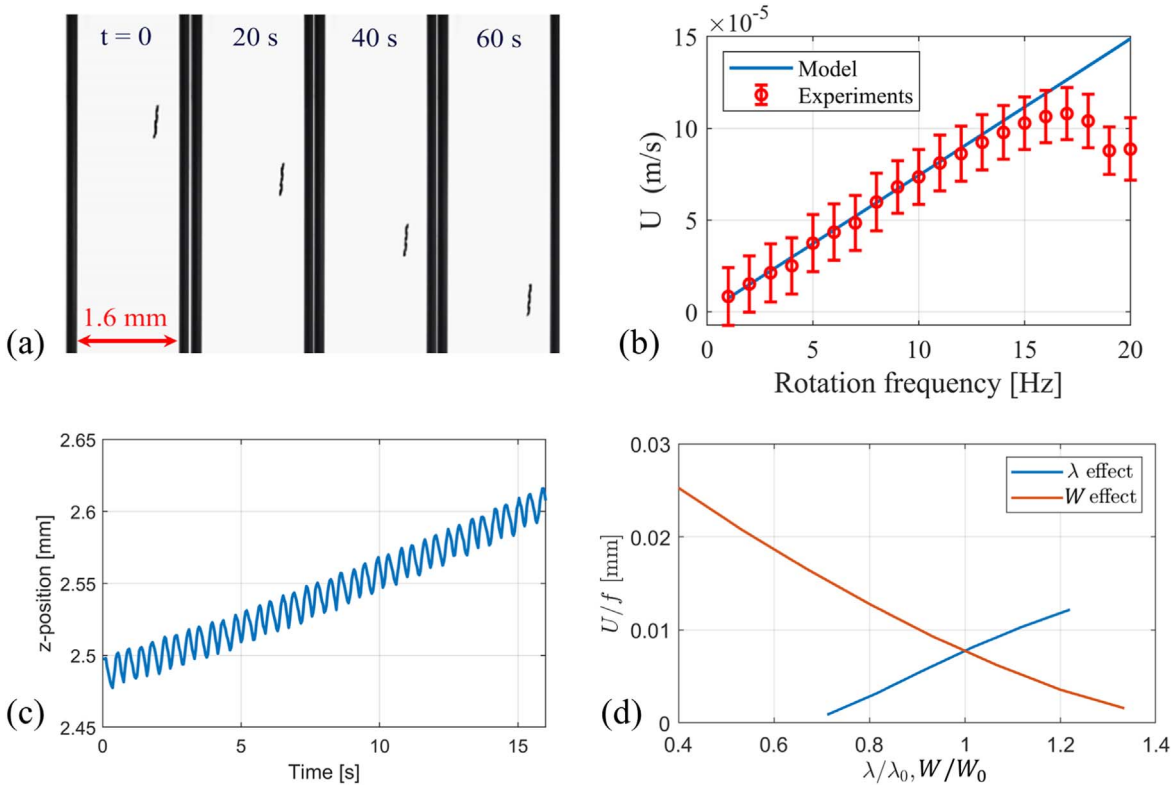

Figure 9. (a) Time-lapse image of the swimmer in a narrow tube under a rotating magnetic field of 5 Hz. (b) The swimming velocities with respect to magnetic rotation frequency. (c) The wobbling trajectory of the swimmer for a magnetic rotation frequency of 1 Hz. (d) Effects of the helical wavelength and the ribbon's width on the swimming stroke, U/f in millimeters.

and reproducibility. As demonstrated by the time-lapse images in figure 9(a), the microswimmer moves alongside the axis of the channel in the vicinity of the wall similar to the behaviour of biological microswimmers [62]. Average swimming velocities from the experiments along the channel's long axis (U) are shown in figure 9(b) and compared with the CFD model results for a swimmer located at 0.5 mm away from the centerline of the channel and rotated around the y- and x- axes by 10° each based on a rough estimate on the swimmer's position and orientation (see section 2.4). Error bars for the experiment results are obtained from the standard deviations. The model agrees well with the experiments for the selected position and orientation of the swimmer. Typically, helical microswimmers demonstrate three modes of swimming: wobbling at low rotation frequencies, followed by cork-screw-like motion at higher frequencies [43, 45, 63]; and step-out when the swimmer fails to rotate synchronously with the magnetic field when the rotation frequency is increased further [46, 51, 63]. As shown in figure 9(b), the swimmer velocity increases linearly with the rotation frequency for up to 17 Hz, reaching a maximum velocity of 110 μm s^{-1}; and, finally, the swimmer enters the step-out region in which the rotation of the swimmer becomes irregular, resulting in a reduced velocity. The three modes of motility at 1 Hz, 7 Hz, and 20 Hz are demonstrated in video S3 in supplemental material and the wobbling trajectory of the swimmer is depicted in figure 9(c). Lastly, the CFD model is used to study the effects of the width and helical wavelength on the stroke of the ribbon swimmer as shown in figure 9(d); the stroke is defined as the distance travelled by each rotation of the helix, and given by U/f. In the plot, W_0 and λ_0 are the width and the wavelength of the helix used in the experiments. Increasing λ decreases swimming speed, whereas increasing W has an opposite effect due to increased resistance of the swimmer. A more comprehensive analysis on the effects of various geometric parameters of helical ribbons on the swimming performance is available in [64].

4. Conclusion

In conclusion, magnetic helical ribbons consisting of a sandwiched nickel nanolayer between two LF-SiN_x and HF-SiN_x layers are successfully manufactured by the strain-induced patterned self-assembly method. The method has key benefits for microswimming applications including improved rigidity, biocompatibility and controllability. Experiments are carried out by varying four geometric parameters of the patterns, which are, width (w), gap (g), depth (H), and the orientation angle (θ), of the patterns, while the ribbon width (W), and length (L) and thicknesses of the layers are kept constant. There is not a straightforward combination that produces desired smooth helical shapes, but for a w/g ratio near 1, low w/L and g/L ratios and high θ give desired results for most of the H/T ratios tested. The rolling process of the top-layer patterned ribbons during etching is modeled using

FEM for the solution of linear elastic equations with moving boundary conditions and large deformations: experiments and model results agree very well even for the cases where the final shape is non-helical. A rotating magnetic field is generated by two pairs of Helmholtz coils to rotate the magnetic helix inside a capillary glass tube filled with isopropyl alcohol to demonstrate the swimming capabilities of the microribbon. The swimming velocity increases steadily up to a rotation frequency of 17 Hz. The similarity of the proposed swimmer design to those used in practical applications should enable easy adoption of the proposed design.

The lifetime of the swimmers, magnetization strength, oxidation resistance and exact measure of biocompatibility could be interesting to study as future work. Moreover, some other methods including magneto acoustic actuation could reduce the wall effects and improve the controllability of the swimmer in various environments. Lastly, to improve the insulation of the magnetic metal from corrosive effects of the aqueous environment, the step coverage method could be incorporated in the PECVD process.

Acknowledgments

The authors thank Dr Cenk Yank and Süleyman Çelik at the SUNUM for assistance in the cleanroom. The research was funded by the Scientific and Technological Research Council of Turkey (TUBITAK), under the Grant No: 116E186.

Data availability statement

The data that support the findings of this study are available upon reasonable request from the authors.

ORCID iDs

Milad Shojaeian https://orcid.org/0000-0003-2394-0970
Hakan Osman Caldag https://orcid.org/0000-0002-4394-6045
Ayhan Bozkurt https://orcid.org/0000-0003-4806-951X
Serhat Yesilyurt https://orcid.org/0000-0001-5425-1532

References

[1] Zhou H *et al* 2021 Magnetically driven micro and nanorobots *Chem. Rev.* **121** 4999–5041
[2] Dong Y *et al* 2022 Magnetic helical micro-/nanomachines: recent progress and perspective *Matter* **5** 77–109
[3] Berg H C and Anderson R A 1973 Bacteria swim by rotating their flagellar filaments *Nature* **245** 380–2
[4] Medina-Sánchez M *et al* 2016 Cellular cargo delivery: toward assisted fertilization by sperm-carrying micromotors *Nano Lett.* **16** 555–61
[5] Li J *et al* 2018 Biomimetic platelet-camouflaged nanorobots for binding and isolation of biological threats *Adv. Mater.* **30** 1704800
[6] Lee S *et al* 2018 Fabrication and characterization of a magnetic drilling actuator for navigation in a three-dimensional phantom vascular network *Sci. Rep.* **8** 1–9
[7] Ullrich F *et al* 2013 Mobility experiments with microrobots for minimally invasive intraocular surgery *Investigative Ophthalmol. Vis. Sci.* **54** 2853–63
[8] Abbott J J *et al* 2009 How should microrobots swim? *Int. J. Robot. Res.* **28** 1434–47
[9] Charon N W *et al* 2012 The unique paradigm of spirochete motility and chemotaxis *Annu. Rev. Microbiol.* **66** 349–70
[10] Nakamura S 2020 Spirochete flagella and motility *Biomolecules* **10** 550
[11] Tahara H *et al* 2018 The mechanism of two-phase motility in the spirochete Leptospira: swimming and crawling *Sci. Adv.* **4** eaar7975
[12] Zhang L *et al* 2009 Artificial bacterial flagella: fabrication and magnetic control *Appl. Phys. Lett.* **94** 064107
[13] Tottori S *et al* 2012 Magnetic helical micromachines: fabrication, controlled swimming, and cargo transport *Adv. Mater.* **24** 811– 816
[14] Ghosh A and Fischer P 2009 Controlled propulsion of artificial magnetic nanostructured propellers *Nano Lett.* **9** 2243–5
[15] Khalil I S M *et al* 2016 Magnetic propulsion of robotic sperms at low-Reynolds number *Appl. Phys. Lett.* **109** 033701
[16] Fan X *et al* 2018 Automated noncontact micromanipulation using magnetic swimming microrobots *IEEE Trans. Nanotechnol.* **17** 666–9
[17] Acemoglu A and Yesilyurt S 2015 Effects of poiseuille flows on swimming of magnetic helical robots in circular channels *Microfluid. Nanofluid.* **19** 1109–22
[18] Peters C *et al* 2016 Degradable magnetic composites for minimally invasive interventions: device fabrication, targeted drug delivery, and cytotoxicity tests *Adv. Mater.* **28** 533–8
[19] Ceylan H *et al* 2019 3D-printed biodegradable microswimmer for theranostic cargo delivery and release *ACS Nano* **13** 3353–62
[20] Chen X-Z *et al* 2019 Magnetically driven piezoelectric soft microswimmers for neuron-like cell delivery and neuronal differentiation *Mater. Horiz.* **6** 1512–6
[21] Xie L *et al* 2020 Photoacoustic imaging-trackable magnetic microswimmers for pathogenic bacterial infection treatment *ACS Nano* **14** 2880– 2893
[22] Huang Z and Bai F 2014 Wafer-scale, three-dimensional helical porous thin films deposited at a glancing angle *Nanoscale* **6** 9401–9
[23] Zhao Y *et al* 2017 Coiled plant tendril bioinspired fabrication of helical porous microfibers for crude oil cleanup *Glob. Challenges* **1** 1600021
[24] Li X *et al* 2020 Growth and stress analyses of vanadium dioxide nanomembranes for controllable rolling *J. Phys. D: Appl. Phys.* **53** 455105
[25] Chun I S *et al* 2010 Geometry effect on the strain-induced self-rolling of semiconductor membranes *Nano Lett.* **10** 3927–32
[26] Huang T *et al* 2014 Grating-structured metallic microsprings *Nanoscale* **6** 9428–35
[27] Tian Z *et al* 2018 Anisotropic rolling and controlled chirality of nanocrystalline diamond nanomembranes toward biomimetic helical frameworks *Nano Lett.* **18** 3688–94
[28] Prinz V Y and Golod S V 2006 Elastic silicon-film-based nanoshells: formation, properties, and applications *J. Appl. Mech. Tech. Phys.* **47** 867–78
[29] Prinz V Y *et al* 2000 Free-standing and overgrown InGaAs/GaAs nanotubes, nanohelices and their arrays *Physica* E **6** 828–31
[30] Dai L and Zhang L 2013 Directional scrolling of SiGe/Si/Cr nanoribbon on Si (111) surfaces controlled by two-fold rotational symmetry underetching *Nanoscale* **5** 971–6

[31] Stoychev G *et al* 2012 Shape-programmed folding of stimuli-responsive polymer bilayers *ACS Nano* **6** 3925–34

[32] Tian Z *et al* 2017 Deterministic self-rolling of ultrathin nanocrystalline diamond nanomembranes for 3D tubular/helical architecture *Adv. Mater.* **29** 1604572

[33] Kue R *et al* 1999 Enhanced proliferation and osteocalcin production by human osteoblast-like MG63 cells on silicon nitride ceramic discs *Biomaterials* **20** 1195–201

[34] Dow H S, Kim W S and Lee J W 2017 Thermal and electrical properties of silicon nitride substrates *AIP Adv.* **7** 095022

[35] Dun H *et al* 1981 Mechanisms of plasma-enhanced silicon nitride deposition using SiH4/N 2 mixture *J. Electrochem. Soc.* **128** 1555

[36] Sang L *et al* 2019 Monolithic radio frequency SiNx self-rolled-up nanomembrane interdigital capacitor modeling and fabrication *Nanotechnology* **30** 364001

[37] Michaels J A *et al* 2019 Effect of perforation on the thermal and electrical breakdown of self-rolled-up nanomembrane structures *Adv. Mater. Interfaces* **6** 1901022

[38] Yang Z *et al* 2020 Monolithic heterogeneous integration of 3d radio frequency l- c elements by self-rolled-up membrane nanotechnology *Adv. Funct. Mater.* **30** 2004034

[39] Huang W *et al* 2018 Three-dimensional radio-frequency transformers based on a self-rolled-up membrane platform *Nature Electron.* **1** 305– 313

[40] Froeter P *et al* 2013 3D hierarchical architectures based on self-rolled-up silicon nitride membranes *Nanotechnology* **24** 475301

[41] Van de Ven E P, Connick I-W and Harrus A S 1990 Advantages of dual frequency PECVD for deposition of ILD and passivation films *7th Int. IEEE Conf. on VLSI Multilevel Interconnection* (IEEE) pp 194–201

[42] Gao W *et al* 2014 Bioinspired helical microswimmers based on vascular plants *Nano Lett.* **14** 305–10

[43] Li J *et al* 2014 Template electrosynthesis of tailored-made helical nanoswimmers *Nanoscale* **6** 9415–20

[44] Li J *et al* 2015 Magneto-acoustic hybrid nanomotor *Nano Lett.* **15** 4814–21

[45] Li T *et al* 2017 Highly efficient freestyle magnetic nanoswimmer *Nano Lett.* **17** 5092–8

[46] Zhang L *et al* 2009 Characterizing the swimming properties of artificial bacterial flagella *Nano Lett.* **9** 3663–7

[47] Walmsley B A *et al* 2007 Poisson's ratio of low-temperature PECVD silicon nitride thin films *J. Microelectromech. Syst.* **16** 622–7

[48] Cardinale G F and Tustison R W 1992 Fracture strength and biaxial modulus measurement of plasma silicon nitride films *Thin Solid Films* **207** 126–30

[49] Zhang L *et al* 2006 Anomalous coiling of sige/si and sige/si/cr helical nanobelts *Nano Lett.* **6** 1311–7

[50] Huang H *et al* 2004 Evaluation of elastic modulus and stress gradient of PECVD silicon nitride thin films *SIF2004 Structural Integrity and Fracture* https://espace.library.uq.edu.au/data/UQ_10092/huang_sif04.pdf?dsi_version=5359556583759cd1a7a5b18e7448131a&Expires=1664896139&Key-Pair-Id=APKAJKNBJ4MJBJNC6NLQ&Signature=QyDJisImLSFu9ShF6A-nqsu26F~w~FS17Lrn7OxrjVinYD1FN8vzCsqj3OLysH0qY-zGaYTS7rSIEPh2gNEt~zssn7U6CqxrM-LbAEHHh6j2CjYtVu6hRLpFSb0foFEewJ6c-W~U4rSge69q2cKGO6gLWaykV20rCdnQv7Yqn~S20RoUgw9FUCnri333rNbXAE~Zz4eKKbLM7fmuhf3gYx9n0ti~AsEtyTaWyqsvug6BBfrC65e6dRBrYRewV0P79qJkVU3ObmIZ6APfsn6imHCSTdzGHIF82XAtwbPrwygAEld6J0Bwmy56eW8g10bv8e7RR-TNR8-PndHjEMMJ~Q__

[51] Tottori S *et al* 2013 Assembly, disassembly, and anomalous propulsion of microscopic helices *Nano Lett.* **13** 4263–8

[52] Mahoney A W *et al* 2011 Velocity control with gravity compensation for magnetic helical microswimmers *Adv. Robot.* **25** 1007– 1028

[53] Caldag H O, Acemoglu A and Yesilyurt S 2017 Experimental characterization of helical swimming trajectories in circular channels *Microfluid. Nanofluid.* **21** 1–13

[54] Cendula P *et al* 2011 Directional roll-up of nanomembranes mediated by wrinkling *Nano Lett.* **11** 236–40

[55] Cendula P *et al* 2009 Bending and wrinkling as competing relaxation pathways for strained free-hanging films *Phys. Rev.* B **79** 085429

[56] Huang W *et al* 2014 Precision structural engineering of self-rolled-up 3D nanomembranes guided by transient quasi-static FEM modeling *Nano Lett.* **14** 6293–7

[57] Servant A *et al* 2015 Controlled *in vivo* swimming of a swarm of bacteria-like microrobotic flagella *Adv. Mater.* **27** 2981–8

[58] Caldag H O and Yesilyurt S 2019 Trajectories of magnetically-actuated helical swimmers in cylindrical channels at low Reynolds numbers *J. Fluids Struct.* **90** 164–76

[59] Chen C *et al* 2018 Effect of topological patterning on self-rolling of nanomembranes *Nanotechnology* **29** 345301

[60] Nishidate Y and Nikishkov G P 2006 Generalized plane strain deformation of multilayer structures with initial strains *J. Appl. Phys.* **100** 113518

[61] Chason E and Guduru P R 2016 Tutorial: understanding residual stress in polycrystalline thin films through real-time measurements and physical models *J. Appl. Phys.* **119** 191101

[62] Luo T and Wu M 2021 Biologically inspired micro-robotic swimmers remotely controlled by ultrasound waves *Lab Chip* **21** 4095–103

[63] Morozov K I and Leshansky A M 2014 The chiral magnetic nanomotors *Nanoscale* **6** 1580–8

[64] Demir E and Yesilyurt S 2017 *J. Fluids Struct.* **74** 234–46